Modelling MR-TADF emitters: excited-state decay rate constants and wavefunction descriptors

Mariana T. do Casal[*], *Youssef Badawy, Daniel Escudero*[*]
Quantum Chemistry and Physical Chemistry Section, Department of Chemistry, KU Leuven, Celestijnenlaan 200f, 3001 Leuven, Belgium

Abstract

Multiresonance thermally-activated delayed fluorescence (MR-TADF) emitters have gained popularity given their potential of attaining negligible singlet-triplet energy gaps, i.e., ΔE_{ST}, without hindering emission, thus increasing the reverse and direct intersystem crossing rates without affecting fluorescence. This is achieved due to the singlet and triplet states' short-range charge transfer character (SRCT). Thus, obtaining quantitative information about SRCT would help developing new MR-TADF emitters. This work studies three different families of MR-TADF emitters: DOBOA, DiKTa and OQAO. First, we compute their adiabatic ΔE_{ST} with four different methods (TDA-CAM-B3LYP, STEOM-DLPNO-CCSD, ADC(2) and SCS-CC2). Then, we compute fluorescence (k_r), direct (k_{ISC}), and reverse (k_{rISC}) intersystem crossing rate constants. For k_r, we assess the effect of different levels of approximations on the rate calculations. We show that k_r do not depend significantly on the different harmonic models (adiabatic Hessian or vertical Hessian), coordinate systems, and broadening widths. Moreover, Herzberg-Teller effects are negligible for k_r but they are the main contribution for k_{ISC} and k_{RISC}. The computed rate constants agree well with the experimental results. Moreover, we propose the use of two wavefunction descriptors – Q_a^t and $\mathrm{LOC_a}$ – based on the 1-particle transition density matrix, which assigns the amount of charge centered on the atoms. We compute these descriptors for three transitions: $S_0 \rightarrow S_1$, $S_0 \rightarrow T_1$, and $S_1 \rightarrow T_1$. For the studied cases, these descriptors are independent of the choice of electronic structure method and optimal geometry. We show that the adiabatic ΔE_{ST} decreases with the increase of $S_1 \rightarrow T_1$ Q_a^t, while ΔE_{ST} increases with an increase of the $S_0 \rightarrow T_1$ Q_a^t. These trends showcase how the Q_a^t values can act as guiding descriptors to design new MR-TADF emitters with small ΔE_{ST} values.

1 Introduction

Thermally-activated delayed fluorescence (TADF) occurs through the thermal population of the singlet excited state manifold from the triplet manifold via reverse intersystem crossing (rISC). Fluorescence in TADF dyes occurs in two different regimes. First, after the system is initially excited and the singlet manifold is populated, i.e., prompt fluorescence generally occurs within 1 to 20 ns. Alternatively, after the system undergoes ISC and rISC, the singlet manifold is repopulated, termed delayed fluorescence, typically occurring in the microsecond timescale.[1] The potential applications of this process are many, particularly in the context of organic light emitting diodes (OLEDs).

Singlet emitters are limited to 25% of internal quantum efficiency due to the formation of 75% triplet excitons after electron-hole recombination, the latter ones typically decaying non-radiatively[2] (for fluorophores) or radiatively (for phosphors) with much longer lifetimes. TADF

emitters received considerable attention in recent years because, despite being simple fluorophores they still enable 100% internal quantum efficiency via recycling the triplet excitons. More in detail, in TADF emitters, the rISC process is fast enough to compete with the nonradiative $T_n \rightarrow S_0$ ISC process (**Figure 1A**).

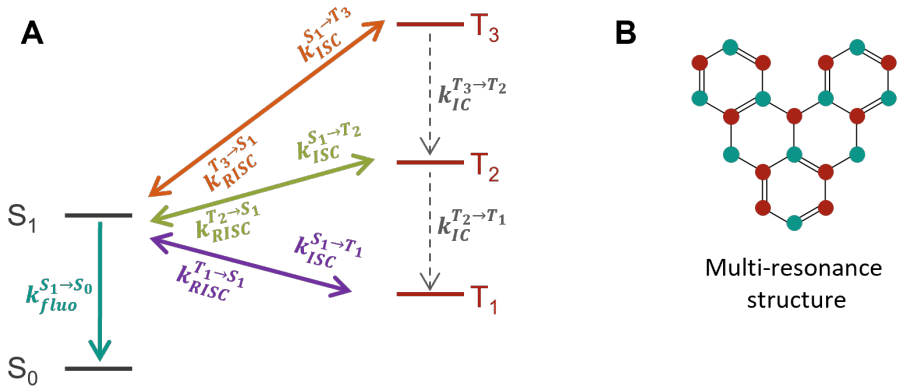

Figure 1 Schematic Jablonski diagram of the possible electronic states involved in thermally-activated delayed fluorescence (A) and typical electron density difference plot of a multi-resonance structure, where red/green indicates an increase/decrease of electronic density, typically observed at the atoms' positions (B).

Often, the bottleneck step for efficient TADF is the rISC process. In order to favor the delayed fluorescence, it is necessary to enhance the rISC rate constant, which, on a simplified picture, depends on the spin-orbit couplings (SOCs) between the involved singlet and triplet excited states and their energy difference, i.e., ΔE_{ST}. ΔE_{ST} is controlled by the sum of the Coulomb electron correlation and the exchange-correlation terms.[3] Early attempts to enhance the rISC relied on diminishing ΔE_{ST} by increasing the charge transfer (CT) character of the involved excited states.[1] An enhanced CT character leads to minimal overlap between the hole and electron densities, which minimizes the exchange interaction energy and, thus, the ΔE_{ST}. However, it also decreases the oscillator strength of the singlet excited state as a side effect, leading to small radiative rate constants. In order to overcome this undesired effect, MR-TADF dyes were designed.[4,5] In MR-TADF dyes, the CT in the relevant singlet and triplet excited states occurs between neighboring atoms, and it is called short-range CT (SRCT, **Figure 1B**). Introducing SRCT has the advantage of decreasing the ΔE_{ST} by minimizing the overlap between the involved excited states. Still some degree of overlap is attained, and this strategy does not fully hinder the oscillator strength.[5] Several MR-TADF emitters fulfilling the above criteria have been proposed. The most widespread design rule involves inserting carbonyl groups, boron and nitrogen atoms in polycyclic aromatic moieties,[4,6–8] among which triangulene-based emitters showed great potential as, for example, DOBOA,[9,10] DiKTa[7,11] and OQOA (see Figure 2).[12] While in DOBOA, the multiresonance effect comes from a polycyclic skeleton containing boron and oxygen atoms, in DiKTa and OQAO, this effect comes from carbonyl groups and nitrogen atoms.

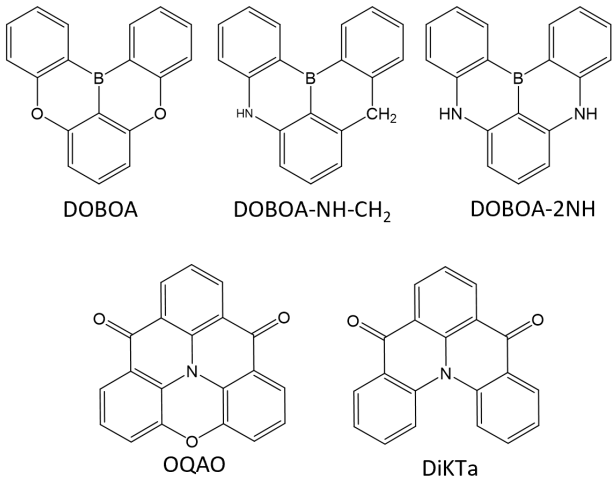

Figure 2 Chemical structures of the molecules studied: DOBOA, DOBOA-NH-CH_2, DOBOA-2NH, DiKTa and OQAO.

Furthermore, the combination of short- and long-range CT effects can synergistically increase the k_{RISC} by introducing a silent CT triplet excited state without affecting the SRCT character of the emissive singlet state.[13–15] This highlights the importance of an in-depth understanding of the mechanisms behind the efficient MR-TADF occurring in these dyes so as to tailor the molecular design strategies by fine-tuning the character and energetic ordering of their excited states. To this end, computational investigations are, thus, key.[1,16–18] As mentioned above, the adiabatic energy gap, i.e., ΔE_{ST}, is the critical factor for the rISC to take place, and it is thus, one of the most commonly used descriptors to predict TADF. To compute the adiabatic ΔE_{ST}, one must obtain the minima of all relevant states, which involve optimizing geometries and obtaining frequencies. When screening a large pool of candidates, this process becomes computationally expensive. Experimentally, obtaining the ΔE_{ST} is not trivial. One common strategy consist of extracting the singlet and triplet energies directly from fluorescence and phosphorescence spectra, respectively.[4,19] However, the lack of fine vibrational structures in the fluorescence spectra of most MR-TADF dyes makes it difficult to identify S_1 energy.[20] Moreover, phosphorescence spectra are usually obtained at lower temperature, which may cause shifts in the spectra compared to room temperature conditions.[1,21] Alternatively ΔE_{ST} can also be obtained from the rate constants dependence on the temperature, an approach which is also prone to errors.[1,22] Besides the ΔE_{ST} and the SOC, the Huang-Rhys factors and thereto the reorganization energies do also strongly impact the ISC rate constants,[23–25] and determine together with the ΔE_{ST} values the activation energy of the $S_1 \rightarrow T_n$ forward and reverse transitions.[26]

Recent advances made the evaluation of excited-state decay rate constants of organic molecular systems possible. The (r)ISC rate constants can be derived from Fermi's golden rule expression, where the Franck-Condon weighted density of states is estimated classically, assuming the high-temperature limit[27] through a semiclassical Marcus rate expression.[28] More elaborated formalisms can also include the effect of vibronic couplings within this framework, i.e., the Marcus-Levich-Jortner formalism.[29,30] However, the above approaches often depart from a one-effective mode treatment only. Alternatively, the excited state decay rate constants, including (r)ISC, can be obtained from vibronic calculations where all vibrational degrees of freedom are explicitly included.[6,8,9,31–34] Vibronic calculations often rely

on the use of the harmonic approximation to describe the potential energy surfaces, and therefore, different models on how to construct these surfaces can be chosen, e.g., adiabatic Hessian vs. vertical Hessian (see Section **¡Error! No se encuentra el origen de la referencia.**). These calculations also strongly depend on other parameters including broadenings, type of coordinates, etc.[32,33,35] In the context of (r)ISC, an extensive assessment of the effect of these parameters was recently done for polyaromatic hydrocarbons,[36,37] but to our knowledge this has not yet been done for MR-TADF emitters.

In the context of MR-TADF emitters, strategies to quantify the SRCT are lacking. In contrast, many descriptors exist to quantify long-range charge transfer during an electronic transition.[38–42] The SRCT character is usually visible from the visual inspection of the density difference between T_1 and S_1,[7,14] frontier molecular orbitals[24] or estimated from $S_0 \rightarrow S_1$ transitions.[23] Visual inspection of orbitals is not ideal when it comes to identifying the most promising candidates in a large pool of molecules since it makes it difficult to differentiate between seemingly similar pictures. A more quantitative analysis was performed by Pershin *et al.*, where they computed the transferred charges, CT volume, CT distance and overlap based on the density difference between ground and excited states.[43] However, this approach does not directly compute these properties based on the transitions between excited states, which are the determining transitions in TADF, but rather computes the transition charges for the $S_0 \rightarrow S_1$ and $S_0 \rightarrow T_x$ transitions. Moreover, the CT distance, that is, the distance between the negative and positive values of the density difference, has shown to the unrealistic assignment of locally excited character in symmetric cases.[44] An alternative strategy is to directly extract information from transition density matrices between the excited states. In this regard, two wavefunction descriptors (Q_a^t and LOC_a, see details in Section 2.1) have been recently proposed by Do Monte *et al*. to account for transition charges in the context of ionic states.[45]

In this work, we investigate the short-range character and rate constants of three MR-TADF emitters (Figure 2): DOBOA,[9,10] DiKTa[7,11] and OQOA.[12] The SRCT character is quantified by the well-defined wavefunction descriptors Q_a^t and LOC_a. While the ΔE_{ST} is particularly sensitive to the choice of electronic structure method, possibly requiring the use of methods that include at least double excitations,[46–49] the effect on the electronic density is less clear[50] in particular for the recently proposed descriptors LOC_a and Q_a^t descriptors. With that in mind, we first assess the impact of four different electronic structure methods on the description of the excited states of DOBOA, DiKTa and OQAO. The choice of electronic structure method is limited given the molecules' size. For that reason, we focus only on TDA-DFT, ADC(2), CC2 and STEOM-DLPNO-CCSD. SCS-CC2 has become the go-to electronic structure method in such cases as it has been shown to provide a good ratio between computational cost and accuracy on the computed ΔE_{ST} values.[8,43] We show how with these descriptors we can easily distinguish the SRCT states for MR-TADF among the triplet manifold. Besides the wavefunction analysis, we compute the relevant fluorescence, ISC and rISC rate constants through vibronic calculations.

2 Theoretical background

2.1 Wavefunction analysis

The 1-electron transition density matrix (TDM) maps a transition between two electronic states according to

$$D_{pq}^{IJ} = \langle \Psi_i | p^\dagger q | \Psi_f \rangle \quad (1)$$

where Ψ_I and Ψ_J are the total wavefunctions of the initial and final states, and $p^\dagger$ and q are the creation and annihilation operators acting on the molecular orbitals. The transition charges on atom *M* are computed from the Löwdin-orthogonalized TDM as

$$q_M^t = \sum_{\mu \in M} \widetilde{D}_{\mu\mu}^t \quad (2)$$

Do Monte *et al.* suggested two descriptors to capture the ionic character in electronic states. In Q_a^t, the absolute values of the transition charges are summed, while in LOC_a the absolute values of the diagonal elements of the TDM are added, according to[45]

$$Q_a^t = \sum_M |q_M^t| \quad (3)$$

$$LOC_a = \sum_\mu \left| \widetilde{D}_{\mu\mu}^t \right| \quad (4)$$

These two descriptors were initially proposed in the context of ionic states in multiconfigurational wave functions. However, these descriptors are essentially measures of charges (in units of *e*) located in the atoms, thus, we propose to use them to also assess SRCT. In MR-TADF emitters, we are interested in transitions between excited states (e.g., S_1 and T_1, T_2, …) and, thus, this analysis should be performed on the TDM that connects the appropriate states. However, it is often the case the electronic structure packages only provide the TDM between S_0 and the excited states ($\boldsymbol{D^{I0}}$ and $\boldsymbol{D^{J0}}$). This limitation can be overcome by a transformation of $\boldsymbol{D^{I0}}$ and $\boldsymbol{D^{J0}}$ into an approximate $\boldsymbol{D_{IJ}}$, as it is implemented in TheoDORE, according to[51]

$$\boldsymbol{D_{IJ}} = \frac{1}{\sqrt{2}} [(\boldsymbol{D^{I0}})^T \boldsymbol{D^{J0}} - \boldsymbol{D^{J0}} (\boldsymbol{D^{I0}})^T] \quad (5)$$

In order to verify the effect of the approximate $\boldsymbol{D_{IJ}}$ on Q_a^t and LOC_a, we obtained the exact and approximate $\boldsymbol{D_{IJ}}$ at TDA-CAM-B3LYP level. Differences on Q_a^t and LOC_a obtained with both approximate and exact $\boldsymbol{D_{IJ}}$ are below 0.1*e* (for a detailed discussion, see Supporting Information, **Table S1**); thus, the approximate $\boldsymbol{D_{IJ}}$ was used for all electronic structure methods.

2.2 Excited State Decay Rate constants

The transition rate between two electronic states (k_{if}) is given by Fermi's golden rule,

$$k_{if} = \frac{2\pi}{\hbar} \left| \langle \Psi_f | \widehat{H}' | \Psi_i \rangle \right|^2 \rho \quad (6)$$

where Ψ_i and Ψ_f are the total wavefunctions of the initial and final states, ρ is the density of states and $\langle \Psi_f | \widehat{H}' | \Psi_i \rangle$ is the perturbation matrix. Applying the Born-Oppenheimer

approximation, i.e., Ψ can be written as the product between electronic (Φ) and vibrational (Θ) wavefunctions, and the Condon approximation, Eq. 6 can be rewritten as

$$k_{if} = \frac{2\pi}{\hbar}\left\langle \Phi_f \middle| \widehat{H}' \middle| \Phi_i \right\rangle^2 \sum_{\nu_i,\nu_f} P_{i,\nu_i}(T) \left| \left\langle \Theta_{i,\nu_i} \middle| \Theta_{f,\nu_f} \right\rangle \right|^2 \delta\left(E_{i,\nu_i} - E_{f,\nu_f}\right) \quad 7$$

where the summation runs over all vibrational states of the initial and final electronic states.[35] The computational cost of including all vibrational states can become unfeasible for larger molecules. A way of avoiding this issue is via a Fourier transformation of this problem to the time domain, called the time-dependent (TD) approach, while solving this summation is called the time-independent (TI) approach. Although the TD approach is less costly, it loses information about the specific contribution of each of the normal modes to the rate constant.

Another challenge in calculating excited state decay rate constants is how to fully describe the potential energy surfaces (PES). The usual strategy is to assume that the PES can be approximated by parabolas, that is, applying the harmonic approximation.[52] This expansion can be done by choosing different geometries as reference points. The two most common choices lead to the adiabatic (AH) and vertical Hessian (VH), models used in this work. In the VH model, the PES of both initial and final states are expanded around the equilibrium geometry of the initial state, while in AH models, the PESs are expanded around the equilibrium geometry of each state. In both models, the Hessian of each state is computed at their corresponding optimized geometries. Other more approximate methods could use the same Hessian for both states, leading to other models (e.g., vertical gradient and adiabatic shift), which are not considered in this work.

The choice of coordinate system can also affect the rate constant calculations. Cartesian coordinates have the advantage of being unambiguously defined. They can lead to unphysical imaginary frequencies around geometries that are not minima in the PES.[52]

Finally, the perturbation $\widehat{H}'$ is chosen to describe the nature of the electronic transition, that is, the perturbation is given by the transition dipole moment ($\vec{\mu}_{ij}$) for radiative transition, while it is given by the SOC ($\widehat{H}_{SOC}$) for an (r)ISC process. Besides the purely electronic contribution to these operators (first term of Equations 8 and 9), one could expand them in terms of the normal vibrational modes, as in

$$\vec{\mu}_{uj}(\vec{Q}) = \vec{\mu}_0 + \sum_k \left(\frac{\partial \vec{\mu}_{ij}}{\partial Q_k}\right)_0 Q_k \quad 8$$

for the transition dipole moment,[53] and

$$\widehat{H}_{SOC}(\vec{Q}) = \left\langle \Psi_{S_i} \middle| \widehat{H}^0_{SOC} \middle| \Psi_{T_f} \right\rangle + \sum_k \partial \frac{\left\langle \Psi_{S_i} \middle| \widehat{H}^0_{SOC} \middle| \Psi_{T_f} \right\rangle}{\partial Q_k} Q_k \quad 9$$

for the SOC operator.[54] The purely electronic contribution is referred to as the Franck-Condon (FC) approximation, and the respective excited-state rate constant (k^{FC}) only takes into account this term of the expansion. On the other hand, the dependency of both operators on the vibrational degrees of freedom is referred to as Herzberg-Teller (HT) effects (second term in Equations 3 and 4). Rate constants that include HT effects are referred to as k^{FCHT} since they also automatically include two contributions, the electronic (FC) and vibrational (HT) contributions.

3 Computational details

The optimization of the ground and (excited state) geometries was performed with (time-dependent) density functional theory level within the Tamm-Dancoff approximation (TDA)[55] using the CAM-B3LYP functional and 6-31++G** level of theory. Geometry optimization included Grimme's dispersion correction,[56] and the minima were confirmed by frequency calculations at the optimized geometries. Single point excited-state energies were also obtained at the second-order algebraic diagrammatic construction method (ADC(2)),[57,58] couple cluster singles and doubles (CC2)[57,59] and similarity transformed equation-of-motion coupled cluster with the domain-based local pair natural orbital approximation (STEOM-DLPNO-CCSD).[60] STEOM-DLPNO-CCSD calculations were done with an occupation of configuration interaction singles natural orbitals cutoff in ionization potential and electronic affinity calculation of 0.001, respectively. At CC2 level, the spin-component scaling (SCS) CC2 were also tested.[61] TDA calculations were performed with Gaussian 16 A.03,[62] while ADC(2) and CC2 calculations were done with TURBOMOLE 7.7.[63]

The calculation of the wavefunction descriptors Q_a^t and LOC_a, as well as the natural transition orbitals was performed with the development version of TheoDORE 3.1.1 software.[51] The descriptors were based on the TDM between the relevant excited states. The excited-state TDMs ($\mathbf{D_{IJ}}$) were computed directly at TDA-CAM-B3LYP level with Gaussian 16 and through the TDMs between the ground state and the respective excited states as implemented in the development version of TheoDORE.

Radiative rate constants were computed with FCClasses3[64] software, and intersystem crossing rate constants were obtained with ORCA 5.0.4.[65]. Emission rate constants were obtained with the FC and FCHT approximations. Both TD and TI formalisms were employed, along with AH and VH models. Additionally, broadenings ranging from 0.001 to 0.5 eV were used to calculate the spectra. ISC rate constants were obtained only with the AH model and a broadening width of 0.002 eV. The SOC matrix elements were obtained within the spin-orbit mean-field approximation, including an effective potential, 1-electron terms, exact Coulomb terms, analytic exchange terms, local DFT correlation[66] and computed at the T_1 and S_1 minimum for reverse and direct ISC, respectively A higher DFT integration grid ('defgrid3') was used to compute the SOC derivatives. HT effects were included in the ISC rate constant calculations (see section 2.2), and the average ISC rate constant for the three spin sub-states $M_s = -1,0,1$ was derived. Duschinsky rotation effects were included. Temperature was set to 298K, and Cartesian coordinates with Lorentzian broadening (FWHM of 10 cm^{-1}) were used for the latter calculations. All vibronic calculations require the Hessian matrix, which was always computed at TDA-CAM-B3LYP level. Energies were computed with different electronic structure methods, as indicated above. The continuum polarizable model was used to include solvation effects,[67] where dicloromethane was used for DOBOA and its derivatives, and toluene was used for OQAO and DiKTa, because their available experimental data were obtained in the above mentioned solvents.

4 Results and Discussion

4.1 Excitation energies

First, we present a benchmark study in the smallest system, DOBOA, to assess which level of theory provides the best compromise between computational cost and accurate energy gaps to use it for the larger compounds. In **Table 1,** the absorption and emission energies for S_1,

along with ΔE_{ST} values of DOBOA are shown. All methods predict S_1 as the bright state (f > 0.167). TDA-CAM-B3LYP predicts the experimental emission energy to be 3.85 eV, overestimating the experimental values by 0.74 eV. ADC(2) and SCS-CC2 predict lower emission energies (3.48 and 3.51 eV, respectively), being ca. 0.4 eV off from the experimental value, while the STEOM-DLPNO-CCSD emission energy (3.29 eV) is only 0.18 eV higher. Regarding the absorption energies, TDA-CAM-B3LYP still leads to the largest difference with the experimental value (4.00 eV compared to the experimental 3.3 eV), while STEOM-DLPNO-CCSD has the best agreement (3.44 eV). SCS-CC2 and ADC(2) predict similar absorption energies (3.67 and 3.64 eV, respectively), approximately 0.3 eV above the experimental value.

In order to discern the states that are more relevant to the TADF process and, thus, build an appropriate excited state kinetic model, we computed the energy of the first three triplet excited states. Their energies computed at the S_1 optimized geometry are generally higher at ADC(2) and SCS-CC2 levels than with TDA-CAM-B3LYP or STEOM-DLPNO-CCSD. This trend is also observed in the T_1 minimum. However, the computed adiabatic ΔE_{ST} values with ADC(2), SCS-CC2 and STEOM-DLPNO-CCSD are very similar (0.19, 0.19 and 0.21 eV, respectively). We recall that accurately calculating the adiabatic ΔE_{ST} values is crucial to obtaining accurate ISC rate constants. Conversely, TDA-CAM-B3LYP predicts a larger ΔE_{ST} compared to the experimental value[10] (0.64 eV compared to 0.15 eV). The zero-point energy correction for the adiabatic ΔE_{ST} was computed at TDA-CAM-B3LYP but it is negligible (approximately 0.02 eV). This result is in line with previous conclusions for similar classes of molecules that TD-DFT methods are generally not appropriate to recover the ΔE_{ST} values of MR-TADF emitters.[43]

Table 1 Transition energies (eV) and oscillator strengths (*f*) of DOBOA at S_0, S_1 and T_1 minima ($S_{0\text{-min}}$, $S_{1\text{-min}}$ and $T_{1\text{-min}}$, respectively) at TDA-CAM-B3LYP, SCS-CC2, CC2, ADC(2) and STEOM-DLPNO-CCSD levels. [a] Experimental values from Ref. 10

	TDA-CAM-B3LYP		**SCS-CC2**		**ADC(2)**		**STEOM-DLPNO-CCSD**		**Exp.[a]**
	EE	***f***	**EE**	***f***	**EE**	***f***	**EE**	***f***	***EE***
@$S_{0\text{-min}}$									
S_1	4.00	0.329	3.67	0.175	3.64	0.169	3.44	0.178	3.30
@$S_{1\text{-min}}$									
S_1	3.85	0.305	3.51	0.161	3.48	0.155	3.29	0.167	3.11
T_1	3.17		3.32		3.30		3.09		
T_2	3.67		3.90		3.89		3.33		
T_3	3.75				3.94		3.41		
@$T_{1\text{-min}}$									
T_1	3.17		3.33		3.30		3.08		2.97
$\Delta E_{S1\text{-}T1}$	0.64		0.19		0.19		0.21		0.15[a]

Based on the results for DOBOA, we now turn the discussion to DiKTa and OQAO. Because of the computational cost of the STEOM-DLPNO-CCSD calculations, we only did TDA-CAM-B3LYP, ADC(2) and SCS-CC2 calculations in these systems. As shown in **Table 2**, TDA-CAM-B3LYP also overestimates the emission energies of S_1 in DiKTa and OQAO (3.40 and 3.04 eV, respectively) by ~0.7 eV compared to the experimental energies (2.69 and 2.38 eV, respectively), while ADC(2) and SCS-CC2 energies are ca. 0.4 eV above the absolute experimental values. Despite this difference, the computed adiabatic ΔE_{ST} values at ADC(2) and SCS-CC2 are only up to 0.04 eV above the experimental ones. The zero-point energy correction for ΔE_{ST} at TDA-CAM-B3LYP is below 0.03 eV in all cases.

In all cases, the key difference between the methods is their estimation of the T_2 and T_3 energies (**Table 1**). For DOBOA, TDA-CAM-B3LYP predicts that T_1, T_2 and T_3 are below S_1, while with STEOM-DLPNO-CCSD, only T_1 and T_2 are lower in energy than S_1. However, T_3 is 0.12 eV above S_1. Based on the STEOM-DLPNO-CCSD results, ISC to T_2 and T_3 are potential alternative deactivation channels (**Figure 1**, orange and green arrows), implying that ISC and IC involving the high-lying triplet states (**Figure 1**, black arrows) may also need to be considered and thus, leading to a complex kinetic model. On the other hand, ADC(2) and SCS-CC2 predict a much higher T_2 state compared to S_1 (0.41 and 0.39 eV, respectively) and, consequently, an even higher T_3 state. Therefore, $S_1 \rightarrow T_2$ and $S_1 \rightarrow T_3$ ISC are likely negligible because of their thermodynamically uphill nature. Thus, we here use a simplified kinetic model where only ISC and rISC between S_1 and T_1 are considered (**Figure 1**, purple arrow). In view of all the

computed evidences the used simplified kinetic model is perdectly suited for DiKTa and OQAO but may likely lead to slightly underestimated $k_{(R)ISC}$ computed values in DOBOA.

Table 2 Transition energies (eV) and oscillator strengths (*f*) of DOBOA at S_0, S_1 and T_1 minima ($S_{0\text{-min}}$, $S_{1\text{-min}}$ and $T_{1\text{-min}}$, respectively) at TDA-DFT/CAM-B3LYP, SCS-CC2, CC2, ADC(2) and STEOM-DLPNO-CCSD levels. [a] Ref.[68] [b] Ref. [12].

	DiKTa						
	CAM-B3LYP		**SCS-CC2**		**ADC(2)**		**Exp.**
	EE	***f***	**EE**	***f***	**EE**	***f***	
$S_{0\text{-min}}$							
S_1	3.57	0.403	3.38	0.195	3.37	0.198	2.86[a]
$S_{1\text{-min}}$							
S_1	3.40	0.376	3.20	0.184	3.19	0.185	2.69[a]
T_1	2.71		2.97		2.97		
T_2	3.20		3.50		3.28		
T_3	3.36				3.35		
$T_{1\text{-min}}$							
T_1	2.67		2.95		2.93		2.49[a]
$\Delta E_{S1\text{-}T1}$	0.71		0.24		0.24		0.20[a]
	OQAO						
$S_{0\text{-min}}$							
S_1	3.24	0.423	3.08	0.223	3.05	0.220	2.54[b]
$S_{1\text{-min}}$							
S_1	3.04	0.391	2.87	0.207	2.84	0.201	2.38[b]
T_1	2.42		2.68		2.66		
T_2	3.03		3.35		3.31		
T_3	3.21		3.42		3.40		
$T_{1\text{-min}}$							
T_1	2.42		2.70		2.67		2.18[12]
$\Delta E_{S1\text{-}T1}$	0.63		0.19		0.17		0.16[12]

4.2 Excited state decay rate constants calculations

TADF emitters rely on the subtle balance between radiative (k_r), direct (k_{ISC}) and reverse intersystem crossing (k_{RISC}). Thus, predicting those rate constants is essential to assess their feasibility of displaying prompt and delayed fluorescence and to design new TADF emitters with tailored properties. In this section, we present the results of the rate constant calculations of DOBOA, DiKTa and OQAO. As discussed above, we depart from a simplified

excited state kinetic model involving only S_1 and T_1. Given this excited state kinetic model, we here focus on the k_r, k_{ISC} and k_{RISC} calculations.

As discussed in Section 0, one must assess a series of parameters to compute excited state decay rate constants. This assessment is needed to guarantee that the required approximations are still valid for the studied systems, while full disclosure of the set of approximations is essential to ensure reproducibility.[35] For instance, the broadening width, PES model and coordinate system are some of these relevant parameters to assess to ensure the stability of the computed results. We briefly discuss the choices used in this work, and all the full tests performed can be found in **Section S2** of the Supporting Information.

First, we discuss the computed k_r values. Employing AH vs. VH results for the studied systems does not significantly lead to different results, as well as when using different coordinate systems. This agreement indicates that the harmonic approximation – required to hold true for these simulations – is valid for the investigated excited state processes and molecular systems.[69] The largest discrepancy comes from the choice of electronic structure methods used to estimate the energy gaps, with TDA-DFT consistently overestimating the k_r values (**Figure 3**), mostly due to the overestimation of the computed S_1 energies. As expected, HT effects are negligible for all three molecules since the S_1 state of all molecules is moderately dipole-allowed (Table 1-2). Below, we will discuss the k_r values obtained with our best theoretical set of parameters.

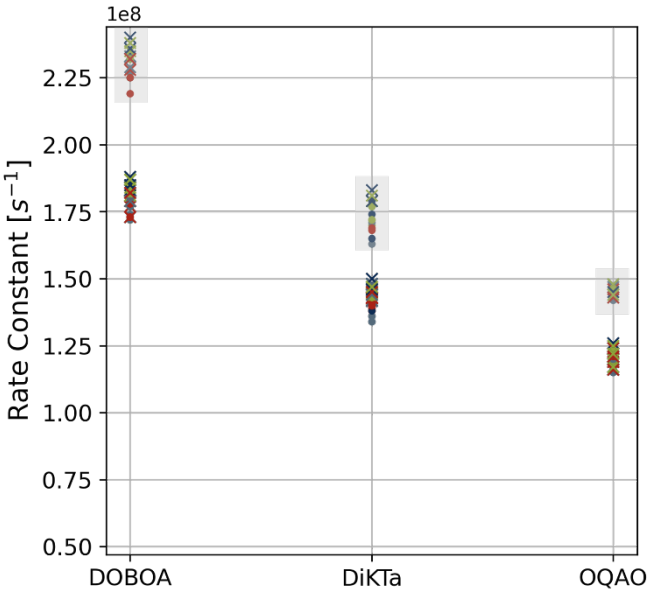

Figure 3 Computed k_r values (s^{-1}) of DOBOA, DiKTa and OQAO with a broadening width of 0.02 eV, adiabatic (circle) and vertical (cross) Hessians, TD/FC (gray), TD/HT (blue), TI/FC (red) and TI/HT (green). TDA results are highlighted in gray.

Figure 4A shows the dependency of the k_r values of DOBOA on the broadening with different approximations (e.g., PES model, coordinate systems and dipole moment model), where the variation between the rate constants is within 0.2 x 10^8 s^{-1} only. Especially up to around 0.3 eV broadening width, the differences between the rate constants within a given set of approximations are mostly independent of the broadening width. The computed spectra show a 0.4 eV blue shift compared to the experimental spectrum as a result of SCS-CC2 predicting a larger emission energy. Despite this shift, the computed spectra recover well the shape of the emission band as seen in the fluorescence spectra in **Figure 4B**, although the

broadening widths assessed are not able to fully recover the experimental broadening. The source of this discrepancy can be attributed, for instance, to other sources of broadening not included in our models, including the specific solvent interactions that are not being taken into account with implicit solvation and dynamic interactions.[70] A similar behavior is also seen in DiKTa and OQAO (**Figure S12** and **S15** of the Supporting Information).

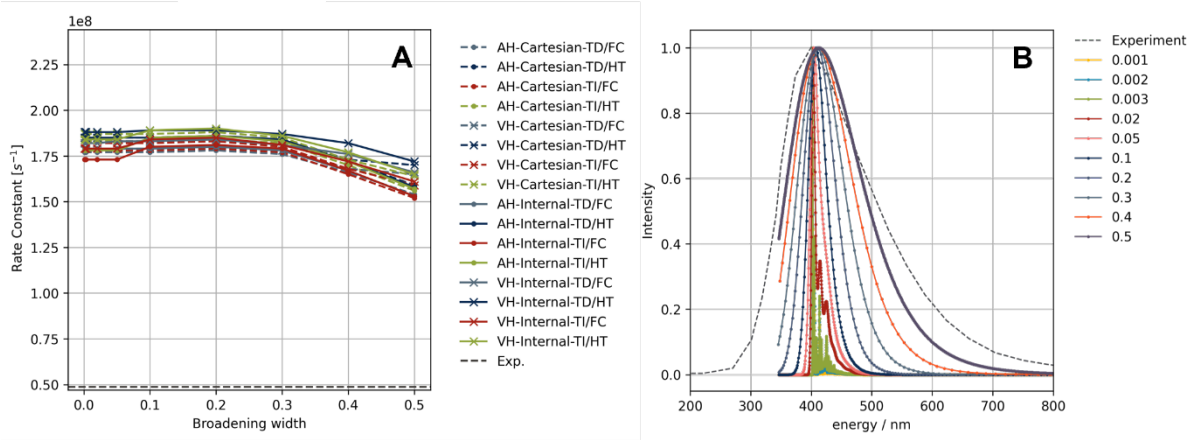

Figure 4 Computed k_r values of DOBOA with different approximations (A) and shifted fluorescence spectra of DOBOA within the Franck-Condon approximation, vertical Hessian model, and time-independent approach (B) at SCS-CC2 level at different broadening widths. Experimental data from Ref. 10.

Now, we turn to the discussion of the ISC rates. All (r)ISC rate constants were computed with the AH model, as this is the only PES model implemented for these type of calculations. HT effects do have a big impact on the computed ISC rate constants. Organic molecules not bearing heavy atoms have markedly small, purely electronic spin-orbit couplings between the singlet and triplet manifolds. Therefore, the largest contribution to the (r)ISC rate comes from the vibrational SOCs. For DOBOA and OQAO, this contribution is almost 100% of the computed k_{ISC} and k_{RISC} (**Table S5** in the Supporting Information). For DiKTa, the electronic SOC is 100 times larger than for DOBOA and OQAO, so the contribution of the HT terms is slightly lower (96% for the k_{ISC} and 91% for k_{RISC}).

In Table 3, we show the computed k_{ISC} and k_{RISC} values for DOBOA, DiKTa and OQAO. For DOBOA, the computed ISC (1.27 x 10^5 s^{-1}) and rISC (1.71 x10^3 s^{-1}) rate constants are smaller than the experimental ones (1.90 x 10^6 s^{-1} for ISC, and 1.55 x 10^4 for rISC), possibly due to omission of alternative deactivation channels that were not considered in our simplified kinetic model (we recall that for DOBOA, T_2 is located below S_1 with STEOM-DLPNO-CCSD). The computed rate constants for DiKTa's rate are slightly larger as compared to the experimental ones, but are accurately predicted within less than one order of magnitude. The difference between the computed and experimental rates is larger than the fluctuations observed due to the different models used. Furthermore, the experimental trend is somewhat recovered with $k_{RISC} < k_{ISC} \ll k_{fluo}$, so that successful predictions of TADF behavior can be derived from our calculations. All in all, there is a good agreement between the computed and experimental rate constants. Although OQAO does not have rates reported experimentally, its potential as TADF emitter has been identified.[12] Moreover, the trend in the computed rate constants of OQAO is similar to that of DiKTa, suggesting also a successful capability of our protocols to predict TADF behavior.

Table 3 Fluorescence (k_r), direct and reverse intersystem crossing rate constants (k_{ISC} and k_{RISC}) in s^{-1}. Fluorescence rates with only the Franck-Condon (FC) contribution and including the Herzberg-Teller (FCHT) are also shown. ISC rates include the HT effects at the SCS-CC2 level. Experimental results, when available, are shown in parentheses.

	DOBOA	**DiKTa**	**OQAO**
k_r^{FC}	1.77 x 10^8 (4.88 x 10^7)	1.43 x 10^8 (4.90x10^7)	1.21 x 10^8
k_r^{FCHT}	1.83 x 10^8	1.45 x 10^8	1.23 x 10^8
k_{ISC}^{FCHT}	1.27 x 10^5 (1.90 x10^6)	2.56 x 10^7 (7.50 x 10^6)	2.10 x 10^6
k_{RISC}^{FCHT}	1.71 x 10^3 (1.55 x 10^4)	6.16 x 10^4 (4.60 x 10^4)	2.17 x 10^4

4.3 Wavefunction analysis

We now turn the discussion to the wavefunction descriptors. The SRCT character can be traced back by visual inspection of the electron density difference plots between the involved singlet and triplet excited states (**Figure 5**). Although visual inspection is sufficient to identify a potential SRCT character, it does not allow for a quantitative comparison between different molecules or the different excited states of a molecule. As mentioned above, we propose using the transition density matrix to obtain a quantitative analysis of the transition process (see **Section 2**). LOC_a and Q_a^t are two descriptors that provide the amount of transition density located on the atoms, allowing the identification of SRCT states. Note that this analysis is performed in the transition density matrix connecting S_1 and each of the involved triplet states, providing relevant information about each possible ISC process, which is not commonly done.

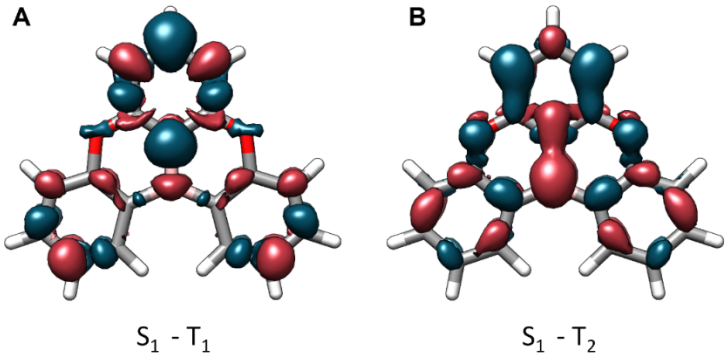

Figure 5 Density difference plot of the $S_1 \rightarrow T_1$ (a) and $S_1 \rightarrow T_2$ (b) of DOBOA. Red indicates positive density, and blue indicates negative density.

In **Table 2**, we show the values of LOC_a and Q_a^t for DOBOA at different levels of theory and for the different ISC channels. We computed both descriptors with different electronic methods from the transition density matrix between S_1 and the three triplet states (T_1/T_2/T_3) to capture the changes in the electron density during the ISC process. First, we notice that there is a clear difference between the Q_a^t and LOC_a values obtained for the $S_1 \rightarrow T_1$ and $T_1 \rightarrow S_1$ ISC processes

(> 1), and those calculated for the $S_1 \rightarrow T_2/T_3$ ISC processes (< 0.5). According to Ref. 45, these values indicate an ionic character to $S_1 \rightarrow T_1$ transition, but covalent regarding T_2/T_3. Moreover, we see that the largest difference in Q_a^t and LOC_a across different levels of theory is only 0.031 and 0.039, respectively (see **Table 4**). The difference in the values comes from the transition charges, where summation terms can cancel each other within a given atom.[45] Since Q_a^t sums over the absolute value of the transition charges, and LOC_a directly sums over the absolute value of the diagonal elements of the TDM. Thus, these cancellations only affect Q_a^t. For DOBOA, this difference in how the descriptors are calculated does not cause a large discrepancy between them.

The consistency among different electronic structure methods suggests that a cheaper method (e.g., TDA-CAM-B3LYP) could be used to screen candidates with potential SRCT character for MR-TADF emitters. Also, we computed those descriptors at S_0 and S_1 minimum geometries (**Table 4** and **Tables S1-2** of the Supporting Information) to address the effect of choosing a different geometry, but it only showed a negligible effect on the descriptors. This result is not unexpected since the molecules are rigid and do not change their electronic properties substantially when relaxing to the excited-state minima, which are common features of MR-TADF emitters. In this case, the descriptors could be obtained from the ground state geometry, avoiding the computational cost of optimizing excited-state geometries.

Table 4 LOC_a and Q_a^t values for the $S_1 \rightarrow T_x$ transition of DOBOA at SCS-CC2, CC2 and ADC(2) with def2-TZVP basis set, and TDA-CAM-B3LYP/6-31++G**.

	$T_1 \rightarrow S_1$ @T_1		$S_1 \rightarrow T_1$ @S_1		$S_1 \rightarrow T_2$ @S_1		$S_1 \rightarrow T_3$ @S_1	
	Q_a^t	LOCa	Q_a^t	LOCa	Q_a^t	LOCa	Q_a^t	LOCa
TDA-CAM-B3LYP	1.124	1.307	1.146	1.306	0.195	0.271	0.408	0.457
SCS-CC2	1.132	1.290	1.127	1.317	0.342	0.457	0.233	0.343
CC2	1.155	1.340	1.166	1.357	0.432	0.545	0.453	0.553
ADC(2)	1.151	1.340	1.167	1.354	0.438	0.554	0.430	0.528

The descriptors agree with the qualitative picture obtained by the density difference plot between the respective states. For instance, **Figure 5a** shows for DOBOA that the density difference between S_1 and T_1 is centered in the atoms, with neighboring atoms showing opposite signs, thus potentially displaying significant SRCT character. On the contrary, the density difference between S_1 and T_2 (see **Figure 5b**) shows that the electron density localizes also through the bonds. On the other hand, the transition charges related to $S_1 \rightarrow T_1$ are shown in **Figure 6c**. Here, the transition charge of each atom is plotted as heat maps, where red and blue indicate negative and positive charges, respectively. Note, however, that the transition charges are calculated for a given atom, so representations such as **Figure 6** do not show the density delocalized through the bonds. Still, **Figure 6** is instructive to identify how the transition charges are localized in the molecule. The SRCT character only comes to light in the $S_1 \rightarrow T_1$ transition (**Figure 6c**), where many neighboring atoms have opposite charges. In the $S_0 \rightarrow S_1$ and $S_0 \rightarrow T_1$ transitions (**Figure 6a and 6b**), the positive and negative charges are localized in different regions of DOBOA.

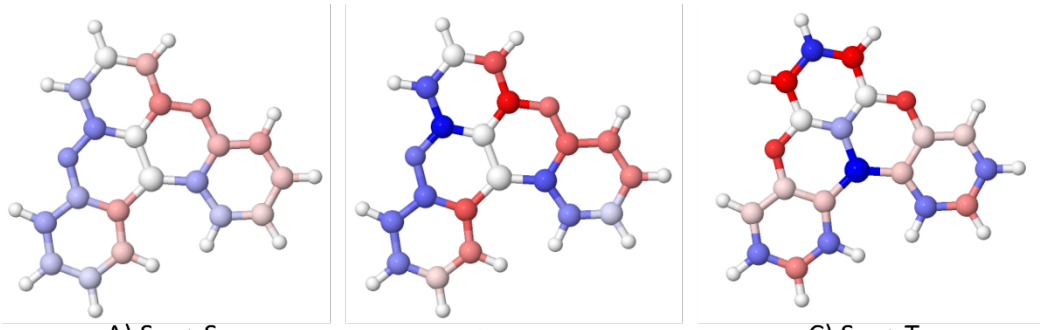

Figure 6 Heat map of the transition charges during $S_0 \rightarrow S_1$, $S_0 \rightarrow T_1$ and $S_1 \rightarrow T_1$ transitions of DOBOA at S_1 geometry and SCS-CC2 level.

This analysis can be extended to other emitters, such as DiKTa and OQAO, showing that the charges are predominantly located on the atoms in the T_1 state (**Table 5**), and the values of the descriptors are similar to those obtained for DOBOA. In **Section S1** of the Supporting Information, we show the density difference plots and transition charges for all molecules.

Table 5 LOC_a and Q_a^t values for the $S_1 \rightarrow T_x$ transition of DOBOA at SCS-CC2 and ADC(2) level.

		$T_1 \rightarrow S_1$ @T_1		**$S_1 \rightarrow T_1$ @S_1**		**$S_1 \rightarrow T_2$ @S_1**		**$S_1 \rightarrow T_3$ @S_1**	
		LOCa	**Q_a^t**	**LOCa**	**Q_a^t**	**LOCa**	**Q_a^t**	**LOCa**	**Q_a^t**
DiKTa	SCS-CC2	1.431	1.129	1.460	1.137	0.293	0.047	0.509	0.339
	ADC(2)	1.460	1.158	1.509	1.184	0.321	0.093	0.286	0.087
OQAO	SCS-CC2	1.217	1.082	1.232	1.106	0.605	0.503	0.302	0.227
	ADC(2)	1.244	1.111	1.260	1.135	0.616	0.527	0.351	0.263

SRCT implies that the density is centered on the atoms and that the neighboring atoms have opposite charges. Q_a^t and LOC_a only inform about the first characteristic, i.e. charges centered on atoms. That is the reason why $S_0 \rightarrow T_1$ Q_a^t (0.87) show similar values to $S_1 \rightarrow T_1$ Q_a^t (1.08), but in the case of the $S_1 \rightarrow T_1$ transition (**Figure 6c**) there is SRCT but not in $S_0 \rightarrow T_1$ (Figure 6b). Hall *et al*. characterize S_1 state of DOBOA and DiKTa as SRCT based on descriptors obtained from the difference density of S_1 and S_0 electronic densities.[36] They compute the overlap between the regions of increased and decreased electronic density (0.92 and 0.91), the distance between the barycentre of the decreased and increased densities (1.57 and 1.45) and the total charge transferred during the transition (0.58 and 0.59), which they suggest is due to SRCT. In the transition density picture used in this work, the SRCT behaviour is more prominent in the $S_1 \rightarrow T_1$ transition.

Note that the adiabatic ΔE_{ST} of DOBOA, DiKTa, and OQAO are spread within a small energetic range (0.19, 0.24 and 0.19 eV at SCS-CC2 level, respectively). Thus, to further explore the possible correlations between the computed descriptors and the adiabatic ΔE_{ST} values, we also calculated the descriptors for two new molecules based on DOBOA (see DOBOA-NH-CH_2 and DOBOA-2NH in **Figure 2**). The adiabatic ΔE_{ST} values of DOBOA-2NH and DOBOA-NH-CH_2 with SCS-CC2 are 0.18 and 0.28 eV, respectively. In Figure 7, we can distinguish two different

tendencies. First, let us look at Q_a^t of the $S_1 \rightarrow T_1$ transition (**Figure 7**, green). We see that there is a somewhat slight tendency for ΔE_{ST} to increase with a decrease in Q_a^t, despite the more pronounced drop of OQAO. This particular behaviour of is also observed in LOC_a (**Figure S8**, Supporting Information), suggesting this drop does not come from a fortuitous cancellation of terms in the summation. In addition, we also see a correlation between Q_a^t of the $S_0 \rightarrow T_1$ transition (**Figure 7**, green) and the adiabatic ΔE_{ST}. The increase of Q_a^t in this transition leads to a increase of the adiabatic ΔE_{ST}, suggesting that an increased ionic character of T_1 can decrease the gap.

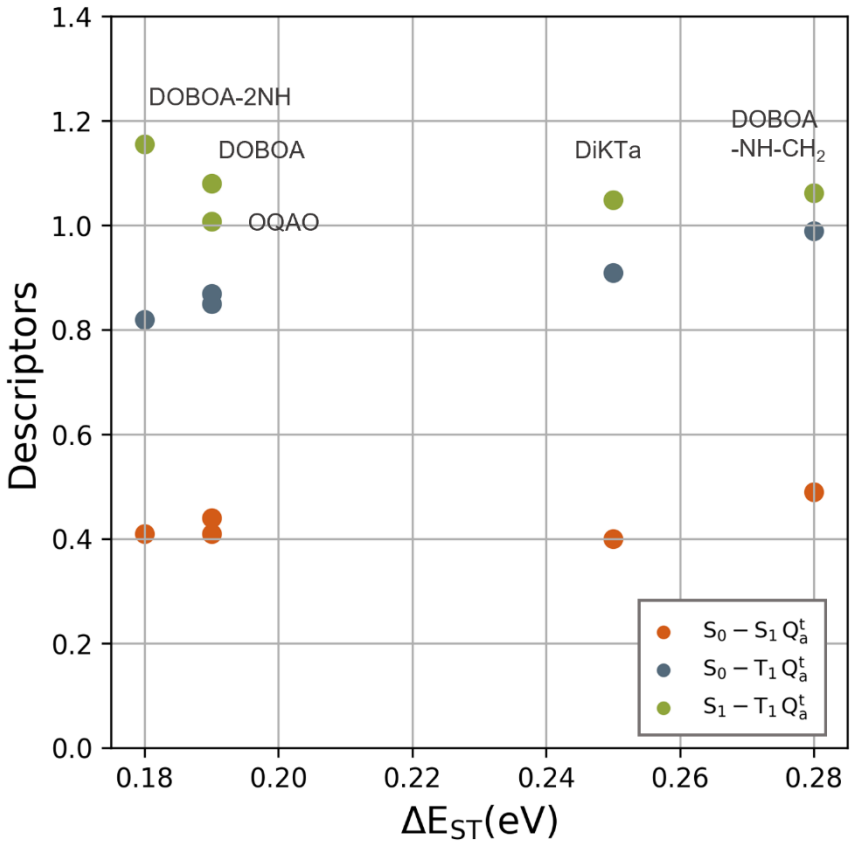

Figure 7 Q_a^t values of different electronic transitions ($S_0 \rightarrow S_1$ / $S_0 \rightarrow T_1$ / $S_1 \rightarrow T_1$) of DOBOA, DOBOA-$2NH_2$, DOBOA-NH_2-CH_2, DiKTa and OQAO at SCS-CC2 level.

5 Conclusion

This work studies three different MR-TADF emitters: DOBOA, DiKTa and OQAO. First, we benchmark the emission, absorption and adiabatic ΔE_{ST} values of DOBOA with four different electronic structure methods: TDA-CAM-B3LYP, STEOM-DLPNO-CCSD, ADC(2) and SCS-CC2. The main quantities to predict excited state rate constants are the SOC and the ΔE_{ST}. Besides TDA-CAM-B3LYP, all methods predict ΔE_{ST} in good agreement with the experimental values. Given the high computational cost of STEOM-DLPNO-CCSD, we chose to focus only on SCS-CC2 energies. We found that at the SCS-CC2 level, T_2 and T_3 are around 0.4 eV above S_1; thus, ISC channels involving S1→T2 and S1→T3 transitions are likely negligible, and a simplified kinetic model involving only S_1 and T_1 states can be used.

Then, we computed k_r, k_{ISC}, and k_{rISC} of DOBOA, DiKTa and OQAO. We assessed the influence in k_r of different PES models (adiabatic vs. vertical Hessian), coordinate systems (internal vs. Cartesian coordinates), broadening widths and transition dipole moment models (Franck-Condon vs. Herzberg-Teller). k_r values do not depend significantly on the PES model or coordinate system for all the investigated molecules. Moreover, Herzberg-Teller effects do not significantly contribute to the fluorescence rate constant. On the other hand, k_{ISC} and k_{rISC} were computed with the adiabatic Hessian model, and Herzberg-Teller terms contribute the most to the rate constant. Overall, DOBOA and DiKTa rate constants agree well with the experimental values, given that they are predicted within one order of magnitude.

Lastly, this work uses two wavefunction descriptors, Q_a^t and LOC_a. Those descriptors have been proposed in the context of ionic states[45] and have been used to obtain a measure of charge centered on the molecule's atoms. They are obtained from the transition density matrix between two excited states. Commonly, this analysis is performed in $S_0 \rightarrow S_n$ or $S_0 \rightarrow T_n$ transitions. Here, however, we analyzed directly the transition density matrix connecting $S_1 \rightarrow T_1$, as well. We compared Q_a^t and LOC_a with TDA-CAM-B3LYP, SCS-CC2 and ADC(2), which suggests that the descriptors are not significantly affected by the choice of electronic structure method. Moreover, the T_1 state of all molecules has LOC_a and Q_a^t above 1, suggesting the a large portion of the transition density is located on the atoms in T_1. In contrast, T_2 and T_3 have LOC_a and Q_a^t below 0.6. According to the classification proposed in ref. [45], T_1 of all molecules are ionic states, while T_2 and T_3 are mostly covalent. This assessment is independent of the electronic structure method chosen, while the adiabatic ΔE_{ST} is highly dependent on this choice. Thus, these descriptors could be obtained at a cheaper electronic structure method such as TDA-DFT and still provide a qualitative measure of the putative SRCT character.

The correlation between the computed wavefunction descriptors and the adiabatic ΔE_{ST} values were investigated. As a proof of principle, we showed that ΔE_{ST} decreases with the increase of Q_a^t related to the $S_1 \rightarrow T_1$ transition. At the same time, ΔE_{ST} increases with an increase in the $S_0 \rightarrow T_1$ Q_a^t while no correlation is seen for $S_0 \rightarrow S_1$ Q_a^t. These tendencies showcase how Q_a^t regarding the S_0 and S_1 transitions to T_1 can act as a guiding descriptor to design new MR-TADF emitters with small ΔE_{ST} values.

Acknowledgments

D.E. acknowledges FWO (project numbers G079122N and G022324N) for financial support. Y.B. acknowledges the financial support of the European Commission for the Erasmus Mundus scholarship.

References

(1) Di Maiolo, F.; Phan Huu, D. K. A.; Giavazzi, D.; Landi, A.; Racchi, O.; Painelli, A. Shedding Light on Thermally-Activated Delayed Fluorescence. *Chem. Sci.* **2024**, 10.1039.D4SC00033A. https://doi.org/10.1039/D4SC00033A.

(2) Hong, G.; Gan, X.; Leonhardt, C.; Zhang, Z.; Seibert, J.; Busch, J. M.; Bräse, S. A Brief History of OLEDs—Emitter Development and Industry Milestones. *Advanced Materials* **2021**, *33* (9), 2005630. https://doi.org/10.1002/adma.202005630.

(3) Silva, P. D. Inverted Singlet-Triplet Gaps and Their Relevance to Thermally Activated Delayed Fluorescence. *The Journal of Physical Chemistry LettersPhysical Chemistry Letters* **2019**, *10*, 5674–5679. https://doi.org/10.1021/acs.jpclett.9b02333.

(4) Hatakeyama, T.; Shiren, K.; Nakajima, K.; Nomura, S.; Nakatsuka, S.; Kinoshita, K.; Ni, J.; Ono, Y.; Ikuta, T. Ultrapure Blue Thermally Activated Delayed Fluorescence Molecules: Efficient HOMO–LUMO Separation by the Multiple Resonance Effect. *Advanced Materials* **2016**, *28* (14), 2777–2781. https://doi.org/10.1002/adma.201505491.

(5) Pershin, A.; Hall, D.; Lemaur, V.; Sancho-Garcia, J.-C.; Muccioli, L.; Zysman-Colman, E.; Beljonne, D.; Olivier, Y. Highly Emissive Excitons with Reduced Exchange Energy in Thermally Activated Delayed Fluorescent Molecules. *Nat Commun* **2019**, *10* (1), 597. https://doi.org/10.1038/s41467-019-08495-5.

(6) Keruckiene, R.; Vaitusionak, A. A.; Hulnik, M. I.; Berezianko, I. A.; Gudeika, D.; Macionis, S.; Mahmoudi, M.; Volyniuk, D.; Valverde, D.; Olivier, Y.; Woon, K. L.; Kostjuk, S. V.; Reineke, S.; Grazulevicius, J. V.; Sini, G. Is a Small Singlet–Triplet Energy Gap a Guarantee of TADF Performance in MR-TADF Compounds? Impact of the Triplet Manifold Energy Splitting. *J. Mater. Chem. C* **2024**, *12* (10), 3450–3464. https://doi.org/10.1039/D3TC04397E.

(7) Wu, S.; Li, W.; Yoshida, K.; Hall, D.; Madayanad Suresh, S.; Sayner, T.; Gong, J.; Beljonne, D.; Olivier, Y.; Samuel, I. D. W.; Zysman-Colman, E. Excited-State Modulation in Donor-Substituted Multiresonant Thermally Activated Delayed Fluorescence Emitters. *ACS Appl. Mater. Interfaces* **2022**, *14* (19), 22341–22352. https://doi.org/10.1021/acsami.2c02756.

(8) Shizu, K.; Kaji, H. Quantitative Prediction of Rate Constants and Its Application to Organic Emitters. *Nat Commun* **2024**, *15* (1), 4723. https://doi.org/10.1038/s41467-024-49069-4.

(9) Cai, W.; Zhong, C.; Wu, D.-Y. Achieving High Color Purity in Multi-Resonance Thermally Activated Delayed Fluorescence Emitters through a Substitution-Driven Design Strategy. *Mater. Chem. Front.* **2023**, *7* (17), 3762–3773. https://doi.org/10.1039/D3QM00280B.

(10) Hirai, H.; Nakajima, K.; Nakatsuka, S.; Shiren, K.; Ni, J.; Nomura, S.; Ikuta, T.; Hatakeyama, T. One-Step Borylation of 1,3-Diaryloxybenzenes Towards Efficient Materials for Organic Light-Emitting Diodes. *Angew Chem Int Ed* **2015**, *54* (46), 13581–13585. https://doi.org/10.1002/anie.201506335.

(11) Hall, D.; Suresh, S. M.; Dos Santos, P. L.; Duda, E.; Bagnich, S.; Pershin, A.; Rajamalli, P.; Cordes, D. B.; Slawin, A. M. Z.; Beljonne, D.; Köhler, A.; Samuel, I. D. W.; Olivier, Y.; Zysman-Colman, E. Improving Processability and Efficiency of Resonant TADF Emitters: A Design Strategy. *Advanced Optical Materials* **2020**, *8* (2), 1901627. https://doi.org/10.1002/adom.201901627.

(12) Zou, S.-N.; Peng, C.-C.; Yang, S.-Y.; Qu, Y.-K.; Yu, Y.-J.; Chen, X.; Jiang, Z.-Q.; Liao, L.-S. Fully Bridged Triphenylamine Derivatives as Color-Tunable Thermally Activated Delayed Fluorescence Emitters. *Org. Lett.* **2021**, *23* (3), 958–962. https://doi.org/10.1021/acs.orglett.0c04159.

(13) Huang, Z.; Xie, H.; Miao, J.; Wei, Y.; Zou, Y.; Hua, T.; Cao, X.; Yang, C. Charge Transfer Excited State Promoted Multiple Resonance Delayed Fluorescence Emitter for High-Performance Narrowband Electroluminescence. *J. Am. Chem. Soc.* **2023**, *145* (23), 12550–12560. https://doi.org/10.1021/jacs.3c01267.

(14) Situ, Z.; Li, X.; Gao, H.; Zhang, J.; Li, Y.; Zhao, F.; Kong, J.; Zhao, H.; Zhou, M.; Wang, Y.; Kuang, Z.; Xia, A. Accelerating Intersystem Crossing in Multiresonance Thermally Activated Delayed Fluorescence Emitters via Long-Range Charge Transfer. *J. Phys. Chem. Lett.* **2024**, *15* (15), 4197–4205. https://doi.org/10.1021/acs.jpclett.4c00608.

(15) Huang, F.; Fan, X.; Cheng, Y.; Xie, Y.; Luo, S.; Zhang, T.; Wu, H.; Xiong, X.; Yu, J.; Zhang, D.; Chen, X.; Wang, K.; Zhang, X. Multiple Resonance Organoboron OLED Emitters with High Efficiency and High Color Purity via Managing Long- and Short-Range Charge-Transfer Excitations. *Advanced Optical Materials* **2023**, *11* (10), 2202950. https://doi.org/10.1002/adom.202202950.

(16) Zhang, Q.; Liu, T.; Shi, Z.; Zheng, Z.; Lv, C.; Wang, X.; Zhang, Y. Narrowband TADF Emitters with High Utilization of Triplet Excitons: Theoretical Insights and Molecular Design. *Phys. Chem. Chem. Phys.* **2024**, *26* (6), 5147–5155. https://doi.org/10.1039/D3CP05439J.

(17) Sanyam; Khatua, R.; Mondal, A. Constructing Multiresonance Thermally Activated Delayed Fluorescence Emitters for Organic LEDs: A Computational Investigation. *J. Phys. Chem. A* **2023**, *127* (49), 10393–10405. https://doi.org/10.1021/acs.jpca.3c05056.

(18) Shizu, K.; Kaji, H. Comprehensive Understanding of Multiple Resonance Thermally Activated Delayed Fluorescence through Quantum Chemistry Calculations. *Commun Chem* **2022**, *5* (1), 53. https://doi.org/10.1038/s42004-022-00668-6.

(19) Liu, Y.; Li, C.; Ren, Z.; Yan, S.; Bryce, M. R. All-Organic Thermally Activated Delayed Fluorescence Materials for Organic Light-Emitting Diodes. *Nat Rev Mater* **2018**, *3* (4), 18020. https://doi.org/10.1038/natrevmats.2018.20.

(20) Dias, F. B. Kinetics of Thermal-Assisted Delayed Fluorescence in Blue Organic Emitters with Large Singlet–Triplet Energy Gap. *Phil. Trans. R. Soc. A.* **2015**, *373* (2044), 20140447. https://doi.org/10.1098/rsta.2014.0447.

(21) Zhang, Q.; Kuwabara, H.; Potscavage, W. J.; Huang, S.; Hatae, Y.; Shibata, T.; Adachi, C. Anthraquinone-Based Intramolecular Charge-Transfer Compounds: Computational Molecular Design, Thermally Activated Delayed Fluorescence, and Highly Efficient Red Electroluminescence. *J. Am. Chem. Soc.* **2014**, *136* (52), 18070–18081. https://doi.org/10.1021/ja510144h.

(22) Hofbeck, T.; Monkowius, U.; Yersin, H. Highly Efficient Luminescence of Cu(I) Compounds: Thermally Activated Delayed Fluorescence Combined with Short-Lived Phosphorescence. *J. Am. Chem. Soc.* **2015**, *137* (1), 399–404. https://doi.org/10.1021/ja5109672.

(23) Li, P.; Zhang, Y.; Li, W.; Zhou, C.; Chen, R. Achieving Narrowband Emissions with Tunable Colors for Multiple Resonance-Thermally Activated Delayed Fluorescence Materials: Effect of Boron/Nitrogen Number and Position. *Phys. Chem. Chem. Phys.* **2023**, *25* (40), 27877–27884. https://doi.org/10.1039/D3CP03781A.

(24) Li, P.; Zhang, Y.; Lv, Q.; Sun, C.; Li, W.; Zhou, C.; Chen, R. Manipulating Multiple Resonance-Charge Transfer Hybrid Proportion for Developing Red Narrowband Thermally Activated Delayed Fluorescence Materials. *J. Phys. Chem. Lett.* **2023**, *14* (38), 8531–8540. https://doi.org/10.1021/acs.jpclett.3c02175.

(25) Zhao, J.; Liu, H.; Fan, J.; Mu, Q. A Molecular Descriptor of a Shallow Potential Energy Surface for the Ground State to Achieve Narrowband Thermally Activated Delayed Fluorescence Emission. *Phys. Chem. Chem. Phys.* **2024**, *26* (6), 5156–5168. https://doi.org/10.1039/D3CP05875A.

(26) Wang, L.; Ou, Q.; Peng, Q.; Shuai, Z. Theoretical Characterizations of TADF Materials: Roles of Δ *G* and the Singlet–Triplet Excited States Interconversion. *J. Phys. Chem. A* **2021**, *125* (7), 1468–1475. https://doi.org/10.1021/acs.jpca.0c09767.

(27) Sanyam; Khatua, R.; Mondal, A. Cost-Effective Approach for Modeling of Multiresonant Thermally Activated Delayed Fluorescence Emitters. *J. Chem. Theory Comput.* **2023**, *19* (24), 9290–9301. https://doi.org/10.1021/acs.jctc.3c01147.

(28) Olivier, Y.; Yurash, B.; Muccioli, L.; D'Avino, G.; Mikhnenko, O.; Sancho-García, J. C.; Adachi, C.; Nguyen, T.-Q.; Beljonne, D. Nature of the Singlet and Triplet Excitations Mediating Thermally Activated Delayed Fluorescence. *Phys. Rev. Materials* **2017**, *1* (7), 075602. https://doi.org/10.1103/PhysRevMaterials.1.075602.

(29) Sidat, A.; Hernández, F. J.; Stojanović, L.; Misquitta, A. J.; Crespo-Otero, R. Competition between Ultralong Organic Phosphorescence and Thermally Activated Delayed Fluorescence in Dichloro Derivatives of 9-Benzoylcarbazole. *Phys. Chem. Chem. Phys.* **2022**, *24* (48), 29437–29450. https://doi.org/10.1039/D2CP04802G.

(30) Ahmed, R.; Manna, A. K. Origins of Molecular-Twist-Triggered Intersystem Crossing in Functional Perylenediimides: Singlet–Triplet Gap versus Spin–Orbit Coupling. *J. Phys. Chem. A* **2022**, *126* (38), 6594–6603. https://doi.org/10.1021/acs.jpca.2c03455.

(31) Pei, Z.; Ou, Q.; Mao, Y.; Yang, J.; Lande, A. D. L.; Plasser, F.; Liang, W.; Shuai, Z.; Shao, Y. Elucidating the Electronic Structure of a Delayed Fluorescence Emitter via Orbital Interactions, Excitation Energy Components, Charge-Transfer Numbers, and Vibrational Reorganization Energies. *J. Phys. Chem. Lett.* **2021**, *12* (11), 2712–2720. https://doi.org/10.1021/acs.jpclett.1c00094.

(32) Lin, S.; Ou, Q.; Shuai, Z. Computational Selection of Thermally Activated Delayed Fluorescence (TADF) Molecules with Promising Electrically Pumped Lasing Property. *ACS Materials Lett.* **2022**, *4* (3), 487–496. https://doi.org/10.1021/acsmaterialslett.1c00794.

(33) Zhang, H.; Ke, L.; Li, Z.; Nie, Y.; Wang, J.; Bi, H.; Wang, Y. Vibronic Transitions Determined Narrowband Emission for Multi-Resonant Thermally Activated Delayed Fluorescence Emitters. *J. Mater. Chem. C* **2023**, *11* (27), 9300–9307. https://doi.org/10.1039/D3TC01355C.

(34) Lüdtke, N.; Kuhnt, J.; Heil, T.; Steffen, A.; Marian, C. M. Revisiting Ligand-to-Ligand Charge Transfer Phosphorescence Emission from Zinc(II) Diimine Bis-Thiolate Complexes: It Is Actually Thermally Activated Delayed Fluorescence. *ChemPhotoChem* **2023**, *7* (1), e202200142. https://doi.org/10.1002/cptc.202200142.

(35) Do Casal, M. T.; Veys, K.; Bousquet, M. H. E.; Escudero, D.; Jacquemin, D. First-Principles Calculations of Excited-State Decay Rate Constants in Organic Fluorophores. *J. Phys. Chem. A* **2023**, *127* (48), 10033–10053. https://doi.org/10.1021/acs.jpca.3c06191.

(36) Veys, K.; Bousquet, M. H. E.; Jacquemin, D.; Escudero, D. *Modelling the Fluorescence Quantum Yields of Aromatic Compounds: Benchmarking the Machinery to Compute*

Intersystem Crossing Rates; preprint; Chemistry, 2023. https://doi.org/10.26434/chemrxiv-2023-1l9cr.

(37) Bousquet, M. H. E.; Papineau, T. V.; Veys, K.; Escudero, D.; Jacquemin, D. Extensive Analysis of the Parameters Influencing Radiative Rates Obtained through Vibronic Calculations. *J. Chem. Theory Comput.* **2023**, *19* (16), 5525–5547. https://doi.org/10.1021/acs.jctc.3c00191.

(38) Le Bahers, T.; Adamo, C.; Ciofini, I. A Qualitative Index of Spatial Extent in Charge-Transfer Excitations. *J. Chem. Theory Comput.* **2011**, *7* (8), 2498–2506. https://doi.org/10.1021/ct200308m.

(39) Etienne, T.; Assfeld, X.; Monari, A. Toward a Quantitative Assessment of Electronic Transitions' Charge-Transfer Character. *Journal of Chemical Theory and Computation* **2014**, *10* (9), 3896–3905. https://doi.org/10.1021/ct5003994.

(40) Guido, C. A.; Cortona, P.; Mennucci, B.; Adamo, C. On the Metric of Charge Transfer Molecular Excitations: A Simple Chemical Descriptor. *J. Chem. Theory Comput.* **2013**, *9* (7), 3118–3126. https://doi.org/10.1021/ct400337e.

(41) Guido, C. A.; Cortona, P.; Adamo, C. Effective Electron Displacements: A Tool for Time-Dependent Density Functional Theory Computational Spectroscopy. *The Journal of Chemical Physics* **2014**, *140* (10), 104101. https://doi.org/10.1063/1.4867007.

(42) Plasser, F.; Lischka, H. Analysis of Excitonic and Charge Transfer Interactions from Quantum Chemical Calculations. *Journal of Chemical Theory and Computation* **2012**, *8* (8), 2777–2789. https://doi.org/10.1021/ct300307c.

(43) Hall, D.; Sancho-García, J. C.; Pershin, A.; Ricci, G.; Beljonne, D.; Zysman-Colman, E.; Olivier, Y. Modeling of Multiresonant Thermally Activated Delayed Fluorescence Emitters–Properly Accounting for Electron Correlation Is Key! *J. Chem. Theory Comput.* **2022**, *18* (8), 4903–4918. https://doi.org/10.1021/acs.jctc.2c00141.

(44) Savarese, M.; Guido, C. A.; Brémond, E.; Ciofini, I.; Adamo, C. Metrics for Molecular Electronic Excitations: A Comparison between Orbital- and Density-Based Descriptors. *J. Phys. Chem. A* **2017**.

(45) Do Monte, S. A.; Spada, R. F. K.; Alves, R. L. R.; Belcher, L.; Shepard, R.; Lischka, H.; Plasser, F. Quantification of the Ionic Character of Multiconfigurational Wave Functions: The Q_a^t Diagnostic. *J. Phys. Chem. A* **2023**, acs.jpca.3c05559. https://doi.org/10.1021/acs.jpca.3c05559.

(46) Tucker, J. W.; Stephenson, C. R. J. Shining Light on Photoredox Catalysis: Theory and Synthetic Applications. *Journal of Organic Chemistry* **2012**, *77*, 1617–1622.

(47) Dreuw, A.; Hoffmann, M. The Inverted Singlet–Triplet Gap: A Vanishing Myth? *Front. Chem.* **2023**, *11*, 1239604. https://doi.org/10.3389/fchem.2023.1239604.

(48) Loos, P.-F.; Lipparini, F.; Jacquemin, D. Heptazine, Cyclazine, and Related Compounds: Chemically-Accurate Estimates of the Inverted Singlet–Triplet Gap. *J. Phys. Chem. Lett.* **2023**, *14* (49), 11069–11075. https://doi.org/10.1021/acs.jpclett.3c03042.

(49) Monino, E.; Loos, P.-F. Connections and Performances of Green's Function Methods for Charged and Neutral Excitations. *The Journal of Chemical Physics* **2023**, *159* (3), 034105. https://doi.org/10.1063/5.0159853.

(50) do Casal, M. T.; Cardozo, T. M. Impact of Low-Cost Methods in the Description of Excimer and Exciplex Formation: Pyrene–Pyrene and Pyrene–Naphthalene Case Studies. *Theoretical Chemistry Accounts* **2020**, *139* (8), 1–13. https://doi.org/10.1007/s00214-020-02658-0.

(51) Plasser, F. TheoDORE: A Toolbox for a Detailed and Automated Analysis of Electronic Excited State Computations. *Journal of Chemical Physics* **2020**, *152* (8), 084108. https://doi.org/10.1063/1.5143076.

(52) Avila Ferrer, F. J.; Santoro, F. Comparison of Vertical and Adiabatic Harmonic Approaches for the Calculation of the Vibrational Structure of Electronic Spectra. *Phys. Chem. Chem. Phys.* **2012**, *14* (39), 13549. https://doi.org/10.1039/c2cp41169e.

(53) Shuai, Z.; Peng, Q. Excited States Structure and Processes: Understanding Organic Light-Emitting Diodes at the Molecular Level. *Physics Reports* **2014**, *537* (4), 123–156. https://doi.org/10.1016/j.physrep.2013.12.002.

(54) Penfold, T. J.; Gindensperger, E.; Daniel, C.; Marian, C. M. Spin-Vibronic Mechanism for Intersystem Crossing. *Chem. Rev.* **2018**, *118* (15), 6975–7025. https://doi.org/10.1021/acs.chemrev.7b00617.

(55) Hirata, S.; Head-Gordon, M. Time-Dependent Density Functional Theory within the Tamm–Dancoff Approximation. *Chem. Phys. Lett.* **1999**, *314* (3–4), 291–299. https://doi.org/10.1016/S0009-2614(99)01149-5.

(56) Grimme, S.; Antony, J.; Ehrlich, S.; Krieg, H. A Consistent and Accurate Ab Initio Parametrization of Density Functional Dispersion Correction (DFT-D) for the 94 Elements H-Pu. *Journal of Chemical Physics* **2010**, *132* (15), 154104. https://doi.org/10.1063/1.3382344.

(57) Hättig, C.; Hald, K. Implementation of RI-CC2 Triplet Excitation Energies with an Application to Trans-Azobenzene. *Phys. Chem. Chem. Phys.* **2002**, *4* (11), 2111–2118. https://doi.org/10.1039/b110847f.

(58) Trofimov, A. B.; Krivdina, I. L.; Weller, J.; Schirmer, J. Algebraic-Diagrammatic Construction Propagator Approach to Molecular Response Properties. *Chemical Physics* **2006**, *329* (1–3), 1–10. https://doi.org/10.1016/j.chemphys.2006.07.015.

(59) Hättig, C.; Weigend, F. CC2 Excitation Energy Calculations on Large Molecules Using the Resolution of the Identity Approximation. *The Journal of Chemical Physics* **2000**, *113* (13), 5154–5161. https://doi.org/10.1063/1.1290013.

(60) Dittmer, A.; Izsák, R.; Neese, F.; Maganas, D. Accurate Band Gap Predictions of Semiconductors in the Framework of the Similarity Transformed Equation of Motion Coupled Cluster Theory. *Inorg. Chem.* **2019**, *58* (14), 9303–9315. https://doi.org/10.1021/acs.inorgchem.9b00994.

(61) Hellweg, A.; Grün, S. A.; Hättig, C. Benchmarking the Performance of Spin-Component Scaled CC2 in Ground and Electronically Excited States. *Physical chemistry chemical physics : PCCP* **2008**, *10* (28), 4119–4127. https://doi.org/10.1039/b803727b.

(62) Frisch, M. J.; Trucks, G. W.; Schlegel, H. B.; Scuseria, G. E.; Robb, M. A. ; Cheeseman, J. R. ; Scalmani, G.; Barone, V.; Petersson, G. A.; Nakatsuji, H.; Li, X.; Caricato, M.; Marenich, A. V.; Bloino, J.; Janesko, B. G.; Gomperts, R.; Mennucci, B.; Hratchian, H. P.; Ortiz, J. V.;

Izmaylov, A. F.; Sonnenberg, J. L.; Williams-Young, D.; Ding, F.; Lipparini, F.; Egidi, F.; Goings, J.; Peng, B.; Petrone, A.; Henderson, T.; Ranasinghe, D.; Zakrzewski, V. G.; Gao, J.; Rega, N.; Zheng, G.; Liang, W.; Hada, M.; Ehara, M.; Toyota, K.; Fukuda, R.; Hasegawa, J.; Ishida, M.; Nakajima, T.; Honda, Y.; Kitao, O.; Nakai, H.; Vreven, T.; Throssell, K.; Montgomery, J. A., Jr.; Peralta, J. E.; Ogliaro, F. ; Bearpark, M. J.; Heyd, J. J.; Brothers, E. N.; Kudin, K. N.; Staroverov, V. N.; Keith, T. A.; Kobayashi, R.; Normand, J.; Raghavachari, K.; Rendell, A. P.; Burant, J. C.; Iyengar, S. S.; Tomasi, J.; Cossi, M.; Millam, J. M.; Klene, M.; Adamo, C.; Cammi, R.; Ochterski, J. W.; Martin, R. L.; Morokuma, K.; Farkas, O.; Foresman, J. B.; Fox, D. J. Gaussian 16, Revision A. 03, Gaussian, Inc.: Wallingford, CT, 2016. **2016**.

(63) TURBOMOLE V7.7 2022, a Development of University of Karlsruhe and Forschungszentrum Karlsruhe GmbH, 1989-2007, TURBOMOLE GmbH, since 2007; Available from Https://Www.Turbomole.Org.

(64) Cerezo, J.; Santoro, F. FCclasses3: Vibrationally-resolved Spectra Simulated at the Edge of the Harmonic. *Journal of Computational Chemistry* **2023**, *44* (4), 626. https://doi.org/10.1002/jcc.27027.

(65) Neese, F. The ORCA Program System. *WIREs Comput Mol Sci* **2012**, *2* (1), 73–78. https://doi.org/10.1002/wcms.81.

(66) Neese, F. Efficient and Accurate Approximations to the Molecular Spin-Orbit Coupling Operator and Their Use in Molecular g-Tensor Calculations. *The Journal of Chemical Physics* **2005**, *122* (3), 034107. https://doi.org/10.1063/1.1829047.

(67) Mennucci, B.; Cancès, E.; Tomasi, J. Evaluation of Solvent Effects in Isotropic and Anisotropic Dielectrics and in Ionic Solutions with a Unified Integral Equation Method: Theoretical Bases, Computational Implementation, and Numerical Applications. *J. Phys. Chem. B* **1997**, *101* (49), 10506–10517. https://doi.org/10.1021/jp971959k.

(68) Yuan, Y.; Tang, X.; Du, X.; Hu, Y.; Yu, Y.; Jiang, Z.; Liao, L.; Lee, S. The Design of Fused Amine/Carbonyl System for Efficient Thermally Activated Delayed Fluorescence: Novel Multiple Resonance Core and Electron Acceptor. *Advanced Optical Materials* **2019**, *7* (7), 1801536. https://doi.org/10.1002/adom.201801536.

(69) Humeniuk, A.; Bužančić, M.; Hoche, J.; Cerezo, J.; Mitrić, R.; Santoro, F.; Bonačić-Koutecký, V. Predicting Fluorescence Quantum Yields for Molecules in Solution: A Critical Assessment of the Harmonic Approximation and the Choice of the Lineshape Function. *J. Chem. Phys.* **2020**, *152* (5), 054107. https://doi.org/10.1063/1.5143212.

(70) Segarra-Martí, J.; Segatta, F.; Mackenzie, T. A.; Nenov, A.; Rivalta, I.; Bearpark, M. J.; Garavelli, M. Modeling Multidimensional Spectral Lineshapes from First Principles: Application to Water-Solvated Adenine. *Faraday Discuss.* **2020**, *221*, 219–244. https://doi.org/10.1039/C9FD00072K.